# Computational Biomechanics for Investigating Arterial Diseases

Takami Yamaguchi[*1)], Takuji Ishikawa[2)], and Yohsuke Imai[2)]

* Professor
1) Department of Biomedical Engineering, Graduate School of Biomedical Engineering
2) Department of Bioengineering and Robotics, Graduate School of Engineering
E-mail: takami@pfsl.mech.tohoku.ac.jp

## Abstract

I have been investigating the cardiovascular system over micro to macro levels by using conjugated computational mechanics analyzing fluid, solid and bio-chemical interactions. In this article, I introduce our recent researches on a novel hemodynamic index for the initiation of cerebral aneurysms focusing on temporal variation of spatial wall shear stress gradient, malaria-infected red blood cell mechanics using a particle method and confocal micro-PTV measurement of blood flow through a stenosed microchannel.

## 1. Introduction

Human cardiovascular system is always under the integrated nervous and humoral control of the whole body, i.e., in homeostasis. Multiple feedback mechanisms with mutual interactions among systems, organs, and even tissues provide integrated control of the entire body. These control mechanisms have different spatial coverages, from the micro- to macroscale, and different time constants, from nanoseconds to decades. I think that these variations in spatial as well as temporal scales should be taken into account in discussing phenomena in the cardiovascular system.

In this background, we have been investigating the cardiovascular system over micro to macro levels by using conjugated computational mechanics analyzing fluid, solid and bio-chemical mechanics. In the present study, I introduce our recent researches on a novel hemodynamic index for the initiation of cerebral aneurysms focusing on temporal variation of spatial wall shear stress gradient, and malaria-infected red blood cell mechanics using a particle method. In order to confirm the reliability of our numerical results, we developed a confocal micro-PTV system to experimentally measure the blood flow in a micro-channel. We will also introduce the experimental results of blood flow through a stenosed microchannel.

## 2. A Novel Hemodynamic Index for Initiation of Cerebral Aneurysms

Cerebral aneurysm is an extremely important disease on the clinical medicine, since the rupture of the cerebral aneurysm is the most common cause of subarachnoid hemorrhage, well known for its very high mortality. Although how cerebral aneurysms initiate is still unclear, hemodynamics is believed to play a vital role. In this study, we try to identify a possible hemodynamic index for predicting the location of cerebral aneurysm initiation.

### 2.1. Methods

#### 2.1.1. Proposed hemodynamic index

Spatial wall shear stress gradient (SWSSG), which would generate flow-induced tension/compression forces on the endothelial cells (ECs), was suggested to have an important role in aneurysm initiation. Wang *et al.* [1] experimentally observed significant disruption of actin cytoskeleton of the ECs by applying cyclic mechanical stretching. Jamous *et al.* [2] reported that disturbed blood flow might precipitate early morphological change of the EC that leads to the formation of cerebral aneurysms. Thus, based on these observations, we propose a novel index for the initiation of cerebral aneurysms, focusing on temporal variations in hemodynamic tension/compression forces (i.e., SWSSG) on the ECs. This index is named the gradient oscillatory number (GON) and defined as

$$GON = 1 - \frac{\left| \int_0^T \boldsymbol{G} dt \right|}{\int_0^T |\boldsymbol{G}| dt}, \qquad (1)$$

where $\boldsymbol{G}$ is the SWSSG vector and $T$ is one pulse duration of the pulsatile blood flow.

#### 2.1.2. Geometry of the artery model

A patient-specific geometry of human internal carotid artery with an aneurysm was employed. This geometry data was provided by the Virtual Intracranial Stenting Challenge 2007 [3]. We reconstructed an arterial model before aneurysm formation by artificially removing the aneurysm from the original one and by minimizing the elastic energy of the arterial wall, as shown in Fig. 1.

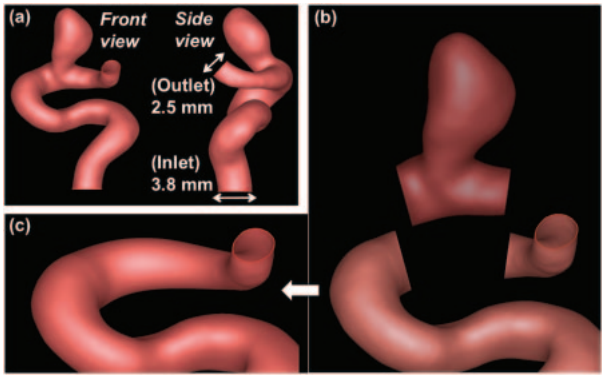


Fig. 1. Construction of the artery model before aneurysm formation. (a) Original patient-specific geometry. (b) Removal of the aneurysm. (c) Smoothing based on the elastic energy minimization.

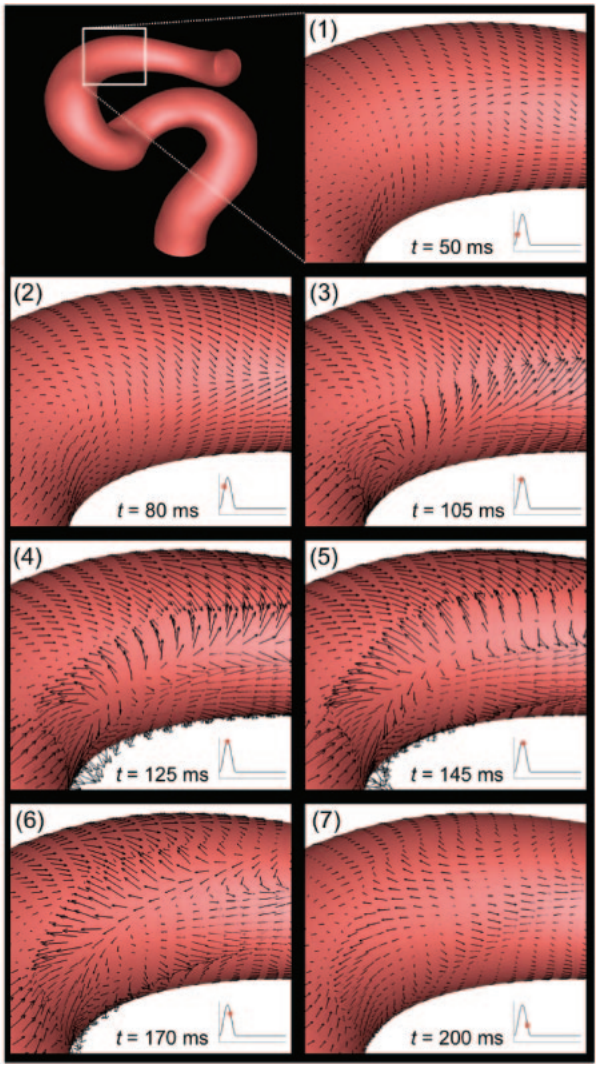


Fig. 2. Temporal variations of the spatial wall shear stress gradient (SWSSG) vector.

### 2.1.3. Blood flow simulations

We performed three-dimensional pulsatile blood flow simulations using an in-house CFD solver to obtain temporal variations in SWSSG vectors and then calculate the GON index. Our CFD solver employed the boundary-fitted coordinate method. The fluid was assumed to be a Newtonian fluid, and a wall was assumed to be rigid. The Womersley number and inlet peak Reynolds number were 2.6 and 300, respectively.

## 2.2. Results and discussion

Figure 2 shows temporal variations of the spatial wall shear stress gradient (SWSSG) vector at the location of aneurysm formation, and the GON index calculated from a set of time-varying SWSSG vectors is shown in Fig. 3. We see that the SWSSG vector

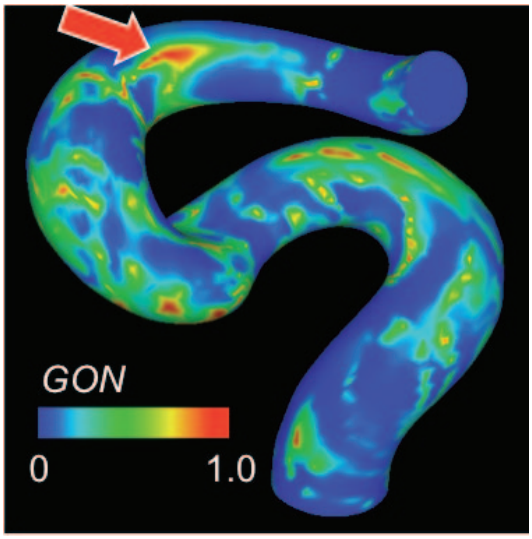


(a) Front view

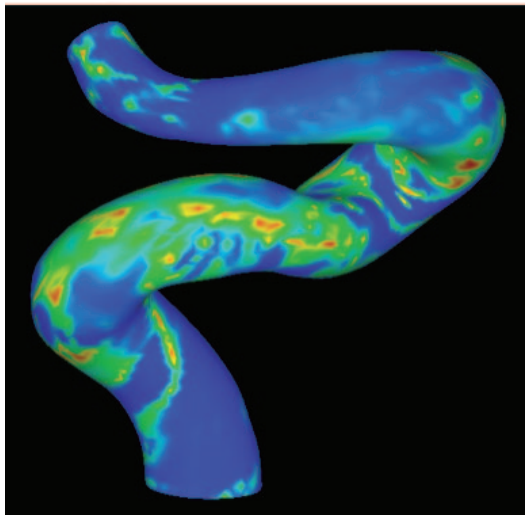

(b) Back view

Fig. 3. Distribution of the GON. (The arrow indicates the location of the aneurysm in the original geometry.)

rotates very strongly over the flow cycle at the location of aneurysm formation. Since the term, $\left|\int_0^T \boldsymbol{G}dt\right|$, in Eq. (1) became nearly equal to zero where strong temporal variations of the SWSSG occurred, the value of GON at the location approached its maximum value (=1).

The SWSSG would generate tension/compression forces (flow-induced forces) on endothelial cells (ECs). Thus, these results indicate that before aneurysm formation strongly disturbed forces were imposed on the ECs there. Recently, Jamous *et al.* [2] reported that such disturbed blood flow might precipitate early morphological change of the EC that leads to the formation of cerebral aneurysm, while we have also demonstrated that disturbed blood flow, i.e. high GON index has a significant correlation with the location of aneurysm formation. Our results support Jamous *et al.*'s findings and suggest that the proposed novel index, GON, may be useful as a hemodynamic index for the initiation of cerebral aneurysms.

## 3. Confocal Micro-PTV Measurement of Blood Flow through Stenosed Microchannel

In a small channel, say 100 μm in diameter, the blood is no longer assumed to be a homogeneous fluid because the size of the blood cells cannot be neglected compared to the generated flow field (the diameter of a RBC is about 8 μm). In such a case, we must treat the blood as a multiphase fluid, and investigate the motion of individual cells in discussing the flow field. Blood can be modeled as a suspension of RBCs in plasma because about 99% of the volume fraction of blood cells consists of RBCs. The interaction of RBCs generates microscale mixing in the blood flow, which has a significant effect on the diffusion of platelets and large molecules. However, numerical simulation of interacting many RBCs is very hard to calculate. Thus, we need to experimental results for checking the reliability of our numerical results.

To measure blood flow experimentally, various methods have been employed. However, observing RBC behavior in the high hematocrit (Hct) blood flow is difficult, since the optical transparency of RBCs can be very low, even if the flow rate is low. To overcome this problem, we developped a confocal micro-PTV (Particle Tracking Velocimetry) system [4]. This system enabled us to visualize the individual RBCs even at high Hct blood (over 10%) by exciting the labeled RBCs with the laser in the system.

In this study, we investigated the motion of RBCs in a microchannel with stenosis using the confocal micro-PTV system. We measured individual trajectories of RBCs around the stenosis under high Hct conditions (up to 20%), when the interactions between RBCs become significant.

### 3.1. Materials and methods

#### 3.1.1. Confocal micro-PTV system

The confocal micro-PTV system used in this study is shown in Fig. 4. Briefly, it consisted of an inverted microscope (IX71; Olympus, Tokyo, Japan), a confocal scanning system (CSU22; Yokogawa, Tokyo, Japan), a high-speed camera (Phantom v7.1; Vision Research, Wayne, NJ, USA), a DPSS laser (Laser Quantum, Cheshire, UK), a syringe pump (KD Scientific, Holliston, MA, USA) for making constant flow, a thermo plate (Tokai Hit, Shizuoka, Japan) for controlling the temperature, and an objective lens (magnification: 20×; N.A.: 0.75; W.D.: 0.17 mm; Olympus). The estimated thickness of the measurement plane (optical slice thickness) was 4.97 μm. By exposing the laser to the labeled RBCs, the system enabled us to track individual RBCs inside the blood flow of up to 20% Hct with high resolution and low optical thickness. The recorded images were evaluated in Image J (NIH, Bethesda, MD, USA) using the manual tracking MtrackJ plug-in.

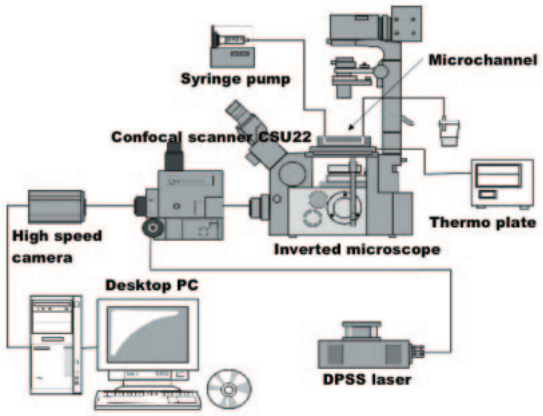


Fig. 4. Experimental set-up

#### 3.1.2. Materials

The microchannel was made of polydimethyl-siloxane (PDMS) using a soft lithographic technique. The microchannel had a square cross section with a side length of 50 μm, and the stenosis was 35 μm high and 30 μm wide, as shown in Fig. 5. The stenosis was 50 μm in depth, so the cross section of the channel in the $x$–$y$ plane did not vary in the $z$-direction. This stenosis geometry was employed so we could clearly observe the effect of stenosis on the blood flow, and the confocal micro-PTV system could accurately measure the motion of RBCs in the center plane.

Four kinds of working fluids were used in this study: pure water with 1% fluorescent particles, 1 μm diameter; dextran 40 (DEX40) with 10% or 20% human RBCs, where 10% of the RBCs were labeled with a fluorescent dye (C-7000; Molecular Probes, Carlsbad, CA, USA); and DEX40 with 10% RBCs that were hardened by a glutaraldehyde treatment [5].

The RBCs were taken from a 23-year-old male volunteer. All procedures were carried out in compliance with the Ethics Committee on Clinical Investigation of Tohoku University.

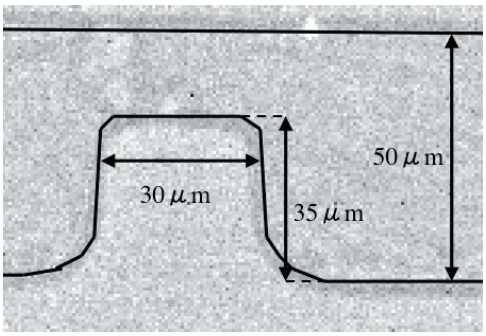


Fig. 5. Stenosis geometry

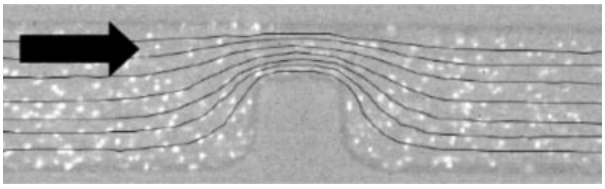

Fig. 6. Trajectories of tracer particles in pure water with 1% fluorescent particles The large arrow in the figure indicates the flow direction

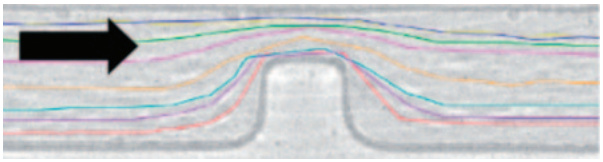

Fig. 7. Trajectories of labeled red blood cells in blood with 10% Hct. The large arrow in the figure indicates the flow direction.

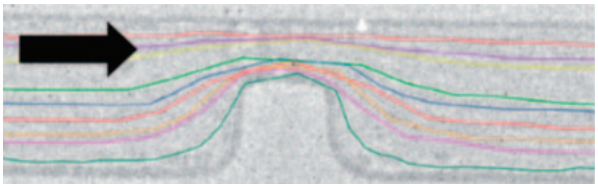

Fig. 8. Trajectories of labeled red blood cells in blood with 20% Hct. The large arrow in the figure indicates the flow direction

### 3.1.3. Experimental conditions

Throughout this study, the average velocity was maintained at about 0.45 mm/s. The Reynolds number, based on the average velocity and the side length of the square cross section, was about 0.02, which was slightly lower than the value of in vivo conditions for small arteries with 50 μm diameter (cf. Popel and Johnson, 2005). Due to the limitation of the PTV system, we could not increase the Reynolds number above 0.02. The microchannel was surrounded by adiabatic walls, and the temperature of the channel was maintained at 37°C by the thermo plate. The frame rate for the high-speed camera was 300 frames per second. Throughout this study, we observed the motion of RBCs in the center plane, i.e. 25 μm from the bottom.

## 3.2. Results

### 3.2.1. Flow of pure water

First, we investigated the flow field of pure water. Fluorescent particles were added to the pure water and visualized by the confocal micro-PTV system. The trajectories of tracer particles were measured by continuously tracking individual particles, as shown in Fig. 6. We observed that the trajectories were almost symmetric between the upstream and the downstream of the stenosis. This result is consistent with the Stokes flow condition, where the streamlines become symmetric if the stenosis shape is symmetric to the *y*-axis.

### 3.2.2. Flow of 10% Hct blood with healthy RBCs

Next, we investigated the blood flow. Labeled RBCs in the blood flow with 10% Hct were visualized at the center plane (i.e. 25 μm depth in the *z*-direction). We observed that the labeled RBCs were visualized clearly. The trajectories of individual RBCs were measured by continuous tracking, and the results are shown in Fig. 7. The trajectories of RBCs were no longer symmetric. RBCs located initially near the lower wall tended to move away from the wall beyond the stenosis. Such a change in position in the *y*-direction was induced by the interaction between the RBC and the stenosis wall. RBCs located initially near the upper wall, however, again tended to move away from the wall beyond the stenosis. This change in position in the *y*-direction was induced by the interaction between the RBC and the upper wall. The *y* position of RBCs changed considerably in the blood flow through the stenosed microchannel.

The asymmetry of the trajectories was induced by the deformation of RBCs. RBCs are deformed by the traction forces generated by the inner- and outer-fluid of the membrane, which depends on the history of deformation along the trajectories. Thus, the deformation of a RBC becomes asymmetric before and after the stenosis, even though the flow field is governed by the Stokes equation. This is the reason why trajectories of RBCs show asymmetry before and after the stenosis.

### 3.2.3. Flow of 20% Hct blood with healthy RBCs

We increased the Hct to 20% and measured the trajectories of labeled RBCs in a blood flow. The

results are shown in Fig. 8. We observed that the trajectories were not as asymmetric as those at 10% Hct. To examine this tendency quantitatively, we measured the RBC displacement in the *y*-direction induced by the flow through stenosis. We define ΔY equal to $Y_{downstream} - Y_{upstream}$, where $Y_{upstream}$ and $Y_{downstream}$ are the *y* position of a labeled RBC 60 μm upstream and downstream of the stenosis, respectively (see Fig. 9). The results at 10% and 20% Hct with various $Y_{upstream}$ are shown in Fig. 10. The error bars indicate standard deviations. In the case of 10% Hct, RBCs near the lower wall (i.e. $Y_{upstream}$ of about 0–10) showed a significant displacement away from the wall. RBCs near the upper wall (i.e. $Y_{upstream}$ of about 40–50) also showed displacement away from the wall (this time, the sign of ΔY was negative). These results indicate that the RBCs tend to flow in the core region of the bulk flow after flowing through the stenosis, although RBCs initially located in the core region do not move significantly in the *y*-direction. In the case of 20% Hct, however, the absolute value of ΔY was much smaller. When Hct was high, the interactions between RBCs increased considerably. Thus, the RBCs cannot concentrate in the core region, but are pushed away from the highly concentrated region due to their interactions. As a result, the displacement of RBCs near the walls may be suppressed more in the case of 20% Hct. Of course, the dispersion of RBCs due to interaction increased as Hct increased, as discussed by Lima et al. [4]. However, the dispersion is isotropic and does not help RBCs to move in one direction.

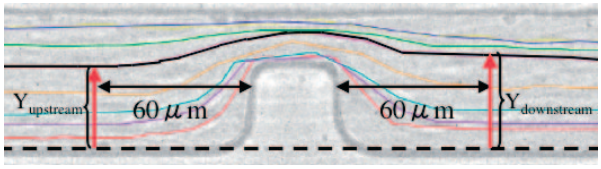


Fig. 9. Definition of $Y_{upstream}$ and $Y_{downstream}$

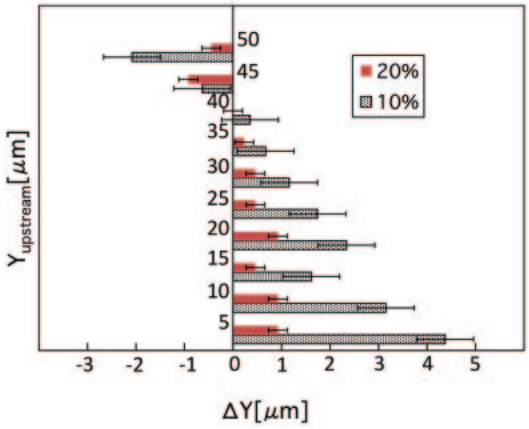


Fig. 10. Effect of Hct and $Y_{upstream}$ on ΔY. The error bars indicate standard deviations.

### 3.2.4. Flow of 10% Hct blood with hardened RBCs

Next, we investigated the blood flow with hardened RBCs to clarify the effect of cell deformability on the blood flow. The RBCs were hardened by a glutaraldehyde treatment. Since the hardened RBCs were not labeled with fluorescent dye, we could not track them under the 10% Hct condition. Instead, we measured the cell-free layer on the upper and lower walls, downstream of the stenosis. The RBCs near the wall could be visualized using a normal halogen light because the concentration of RBCs was low near the wall and the images of RBCs did not overlap very often. Thus, we could measure the distance between the upper or lower wall and the nearest RBC from the wall at 60 μm downstream of the stenosis. By taking the average distance over about 60 RBCs per wall, we calculated the thickness of the cell-free layer. The results are shown in Fig. 11, with error bars indicating the standard deviations. Note that the cell-free layer thickness of healthy and hardened RBCs is about 2–3 μm in the upstream side of the stenosis. We found that the healthy RBCs showed a considerably thicker cell-free layer compared to the hardened RBCs. If RBCs are hardened, the asymmetry in trajectories is no longer enhanced by the deformation of RBCs. Thus, hardened RBCs initially flowing near the wall can stay near the wall, even after flowing through the stenosis. Therefore, we concluded that the deformability of RBCs plays an important role in the blood flow through the stenosis.

## 3.3. Discussion

If one uses a continuum model to analyze the blood flow through a stenosed microchannel, the asymmetry in the flow field in the Stokes flow regime is difficult to express. The Casson model is often used for a constitutive equation of blood, which shows the plasticity and the shear-thinning property of blood. However, the flow field obtained using the Casson model becomes symmetric between upstream and downstream of the stenosis. Although the asymmetry in the flow field can be expressed by employing a constitutive equation for a viscoelastic fluid, the asymmetry in the cell-free layer cannot be expressed. This is because standard constitutive equations assume that the blood is a homogeneous fluid. Therefore, to analyze a blood flow in a small channel (i.e. 50 μm in diameter), one must solve the motion of individual RBCs in the blood.

Faivre et al. [6] investigated blood flow through a microchannel with narrowing to develop a microfluidic device for separating RBCs and plasma. In their experiment, they observed that the thickness of cell-free layer increased as Hct increased. This tendency is the opposite from our observations. We believe that the difference may have been caused by the difference in hematocrit levels used in the two studies; Faivre et al.

used dilute blood (3% Hct), whereas we used more concentrated blood (10% or 20% Hct). In a high Hct blood, the hydrodynamic interactions between RBCs are important, and the behavior of individual RBCs becomes different from that in a low Hct blood. RBCs tend to be pushed away from the concentrated core region when Hct is high, reducing the thickness of the cell-free layer. Another possibility is the difference in stenosis length between the two studies. The stenosis length in this study was 30 μm, or 60% of the channel width. The stenosis length used by Faivre et al. was up to 300 μm, which was three times their channel width. These comparisons indicate that the motion of RBCs may be affected strongly by the Hct and the channel shape.

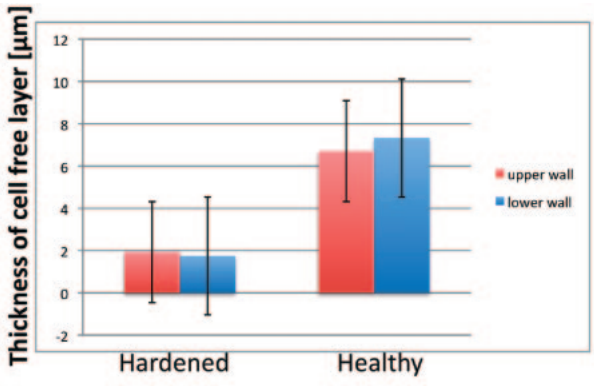


Fig. 11. Effect of the deformability of RBCs on the cell-free layer near the upper and lower wall downstream of the stenosis (Hct = 10%). The error bars indicate standard deviations.

## 4. Malaria

Malaria is one of the most serious infectious diseases on earth. There are 500 million patients with 2 million deaths arising from malaria infection. When a parasite invades and matures inside a red blood cell (RBC), the infected RBC (IRBC) becomes stiffer and cytoadherent. These changes are postulated to link to microvascular blockage [7]. Several researchers have investigated cell mechanics of IRBCs using recent experimental techniques. Methods to quantify the stiffness of the IRBCs include the micropipette aspiration [8-10] and the optical tweezers [11]. Suresh et al. [11] used the optical tweezers to investigate the change of mechanical response of IRBCs at different development stages. They clarified that the shear modules can increase by ten-fold in the final schizont stage. Microfluidics has also been used to investigate the pathology of malaria. Shelby et al. [15] investigated the effect of IRBCs on the capillary obstruction and demonstrated that IRBCs in the late stages of the infection cannot pass through micro channels that have diameters smaller than those of the IRBCs. These studies are reviewed in [12-14].

These experimental studies are still limited to the effect of the single infected cell. However, microvascular blockage may be a hemodynamics problem, involving the interactions between IRBCs, healthy RBCs and endothelial cells. This is due to the limitation of the current experimental techniques. First, it is still difficult to observe the RBC behavior interacting with many other cells even with the recent confocal microscope. Second, the three-dimensional information on flow field is hardly obtained. Third, capillaries in human body are circular channels with complex geometry, but such complex channels cannot be created in micro scale. Instead, numerical modeling can be a strong tool for further understanding the pathology of malaria. Finite element modeling was performed for the stretching of an IRBC by optical tweezers [11]. Dupin et al. [16] also modeled the stretching of the IRBC using lattice Boltzmann method. We have also developed a hemodynamic model involving adhesive interactions [17]. In this section, we present our methodology and preliminary numerical results.

### 4.1. Method

#### 4.1.1. Particle method

Blood is a suspension of RBCs, white blood cells, and platelets in plasma. An RBC consists of cytoplasm enclosed by a thin membrane. Assuming that plasma and cytoplasm are incompressible and Newtonian fluid, the governing equations are described as

$$\frac{D\rho}{Dt} = 0 \,, \tag{2}$$

$$\frac{D\mathbf{u}}{Dt} = -\frac{1}{\rho}\nabla p + \nu\nabla^2\mathbf{u} + \mathbf{f} \,, \tag{3}$$

where the notation $t$ refers to the time, ρ is the density, $\mathbf{u}$ is the velocity vector, $p$ is the pressure, $\nu$ is the dynamic viscosity, $\mathbf{f}$ is the external force per unit mass, and $D/Dt$ is the Lagrangian derivative.

Our model is based on a particle method. All the components of blood are represented by of particles (Fig. 12). Note that each particle is not a real fluid particles but a discrete point for computation. Fluid variables are calculated at the computational point and it is moved by the calculated advection velocity every time step. In conventional mesh methods, each computational point requires the connection to neighboring points for the discretization of Eqs. (2) and (3) and thus the computational meshes are generated. When a red blood cell approaches to other cell, however, the computational meshes can be distorted and destroyed easily. In contrast to mesh methods, the particle method does not require such computational meshes and the computation is stable even when many cells interacting with each other. Another advantage of the particle method is the coupling with the front-tracking. The particle method tracks the front of membrane using the membrane particles and the no-slip condition on the membrane is

directly imposed to Eq. (3) by using the position and velocity of membrane particles. We use moving particle semi-implicit (MPS) method [18] for solving Eqs. (2) and (3). In the MPS method, differential operators in the governing equations are approximated using the weight function, for example,

$$\nabla\phi_i = \frac{d}{n^0}\sum_{j\neq i}\frac{\phi_j-\phi_i}{|\mathbf{r}_{ij}|^2}\mathbf{r}_{ij}w(|\mathbf{r}_{ij}|), \tag{4}$$

$$\nabla^2\phi_i = \frac{2d}{\lambda n^0}\sum_{j\neq i}(\phi_j-\phi_i)w(|\mathbf{r}_{ij}|), \tag{5}$$

where $\phi$ is a fluid variable, $d$ is the space dimension number, $n^0$ is the reference particle number density, $\lambda$ is the constant, $\mathbf{r}$ is the position of particle, $\mathbf{r}_{ij} = \mathbf{r}_j - \mathbf{r}_i$, and $w$ is the weight function.

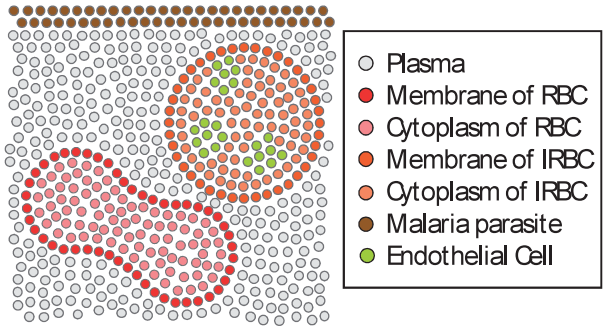


Fig. 12. Schematic of free mesh particle model of blood. All the components of blood are represented by finite number of particles (computational points). Velocity and pressure are calculated at the position of each particle and it is moved by the calculated advection velocity every time step.

### 4.1.2. IRBC model

The membrane of IRBCs is represented by the two-dimensional network consisting of the finite number of particles (Fig. 13). Particle $j$ is connected to particle $i$ by linear spring, giving a force,

$$\mathbf{F}_j^s = k_s(|\mathbf{r}_{ij}| - l_0)\frac{\mathbf{r}_{ij}}{|\mathbf{r}_{ij}|}, \tag{6}$$

where $k_s$ is the spring constant and $l_0$ is the equilibrium distance. A bending force is also considered in our model:

$$\mathbf{F}_j^b = \mathbf{F}_k^b = \frac{\mathbf{F}_i^b + \mathbf{F}_l^b}{2}, \tag{7}$$

$$\mathbf{F}_i^b = k_b\tan\left(\frac{\theta}{2}\right)\mathbf{n}_{ijk}, \tag{8}$$

$$\mathbf{F}_l^b = k_b\tan\left(\frac{\theta}{2}\right)\mathbf{n}_{jkl}, \tag{9}$$

where $k_b$ is the spring constant, $\theta$ is the angle between the triangles $\Delta_{ijk}$ and $\Delta_{jkl}$, and $\mathbf{n}_{ijk}$ is the normal vector to the triangle $\Delta_{ijk}$. The external force per mass is given as

$$\mathbf{f}_i = \frac{\mathbf{F}_j^s + \mathbf{F}_j^b}{\rho V_0}, \tag{10}$$

where $V_0$ is the reference volume $V_0 = r_0^3$, $r_0$ is the averaged particle distance at initial time step. Note that the spring constants $k_s$ and $k_b$ should be model parameters to control the deformation of IRBCs. As described in the next section, we adjust these model parameters through numerical experiments.

A malaria parasite inside IRBCs is modeled by a rigid object constructed by some particles. The treatment of the rigid object in the MPS method was proposed by Koshizuka et al [19].

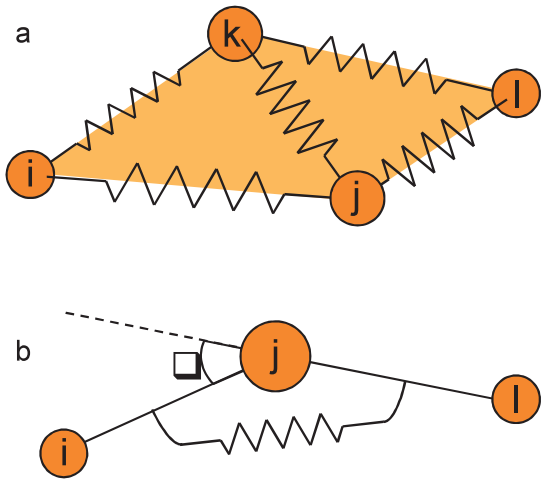


Fig. 13. Spring network model of IRBC membrane. (A) Each membrane particle is connected to negboring membrane particles by a spring with linear elasticity. (B) To express deformation of thin membrane, bending force is also introduced.

### 4.1.3. Time integration

The time step size of time integration is limited by several factors. Most famous one in computational fluid dynamics is the Courant number limitation for the time integration of advection term. In the micro circulation, the diffusion number can be the most serious parameter because of small Reynolds number. Also, the behavior of RBC membrane may limit to the time step size. To avoid the use of small time step size, we employ a fractional time step method with sub time steps. The fractional time step method is written by

$$\mathbf{u}^{*} = \mathbf{u}^{n} + \nu\nabla^{2}\mathbf{u}^{n}\Delta t, \qquad (11)$$

$$\mathbf{u}^{**} = \mathbf{u}^{*} + \mathbf{f}^{*}\Delta t, \qquad (12)$$

$$\mathbf{u}^{n+1} = \mathbf{u}^{**} - \nabla p^{n+1}\Delta t, \qquad (13)$$

where the superscripts $n$ is the time step, $\mathbf{u}^{*}$ and $\mathbf{u}^{**}$ are the intermediate velocity. However, the time step size $\Delta t$ in Eqs. (11) and (12) may be not small enough for the stable computation. Thus we introduce the sub time step, for example,

$$\mathbf{u}^{*} = \mathbf{u}^{n} + \sum_{m=0}^{M-1} \nu\nabla^{2}\mathbf{u}^{n,m}\Delta\tau, \qquad (14)$$

$$\mathbf{u}^{n,m+1} = \mathbf{u}^{n,m} + \nu\nabla^{2}\mathbf{u}^{n,m}\Delta\tau, \qquad (15)$$

where the superscript $m$ is the sub time step, and $\Delta\tau = \Delta t / M$ is the sub time step size. The sub time step size is determined by the diffusion number limitation.

### 4.2. Results

#### 4.2.1. Stretching of IRBCs

Suresh et al. [11] performed stretching of IRBCs by optical tweezers to quantify the mechanical response of IRBCs. They measured the axial and transverse diameters of IRBCs at different development stages with several stretching forces. We examine this stretching test numerically to validate our model. In the three-dimensional computational domain, we put an IRBC at initial time step. Then we stretch the IRBC horizontally with a stretching force as shown in Fig. 14. The governing equations are time-integrated until the axial and transverse diameters are well converged. If the obtained results do not follow the experimental results, the values of model parameters $k_s$ and $k_b$ are changed and the computation is carried out again. Finally we can get the appropriate values of the model parameters. Final results of IRBCs in the schizont stage are presented in Fig. 15. The numerical results agree well with the experimental results by Suresh et al [11].

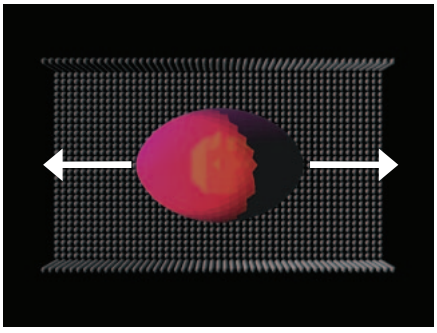

Fig. 14. Stretching of IRBCs. An IRBC is replaced at the center of the computational domain at initial time step. The IRBC is stretched horizontally by a constant force. Governing equations are time integrated until the steady state solution is obtained.

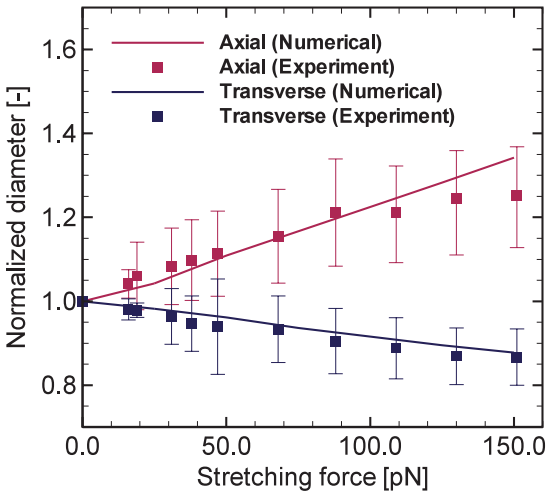


Fig. 15. Comparison between numerical results and experimental results [11] for stretching of IRBCs in schizont stage. Symbols indicate the experimental results and lines are the numerical results. Red is the results for axial diameter and blue is that for transverse diameter. The numerical results agree well with the experimental ones.

#### 4.2.2. Flow in narrow channels

We also simulate the flow into narrow channels using our numerical model. We consider the flow of healthy RBCs (HRBCs) and schizont IRBCs in a 6-μm-square channel and a 4-μm-square channel. The flow is driven by the pressure difference between the inlet and outlet. Figure 16 shows snapshots of the numerical simulation for 6-μm-square channels. As observed in experimental studies, the HRBC passes through the narrow channel with large deformation. The schizont IRBC also deforms and enters the narrow channel. In the case of 4-μm-square channel, the HRBC again largely deforms and passes through the narrow channel. In contrast to the HRBC, the schizont IRBC approaches to the entrance of the narrow channel with small deformation, but cannot flow into the narrow channel.

### 4.3. Discussion

We have proposed a numerical model of three-dimensional hemodynamics arising from malaria infection. A particle based spatial discretization and sub time step time integration method are employed to stably simulate many cell interactions in micro scale blood flow.

To validate our model, we examined stretching of IRBCs. When we used appropriate values for the spring coefficients $k_s$ and $k_b$, the numerical results agreed well with the experimental results. Small differences can be found in the axial diameter for high

stretching force. It may be improved using a non-linear spring model for membrane. However, compared with previously presented numerical models, such as a finite element model [11] and a Lattice Boltzmann model [16], our model has similar accuracy for the stretching of IRBCs.

Our model also successfully simulated flow into narrow channels, mimicking microcirculation in human body. We tested two sizes of narrow channels: a 6-μm-square channel and a 4-μm-square channel. Both HRBCs and IRBCs in the schizont stage passed through a 6-μm-square channel. While HRBCs also flowed into the 4-μm-square channel, schizont IRBCs occluded the flow. These results follow the experimental observation by Shelby et al [15], where they revealed that IRBCs in the late trophozoite and schizont stages occluded flow into the channel with 4μm width. The depth of their channels was fixed to 2μm and thus the effect of such a small depth was not clarified. In contrast to their experiments, our results clearly demonstrated that the IRBCs can occlude the flow even in the 4-μm-square channels.

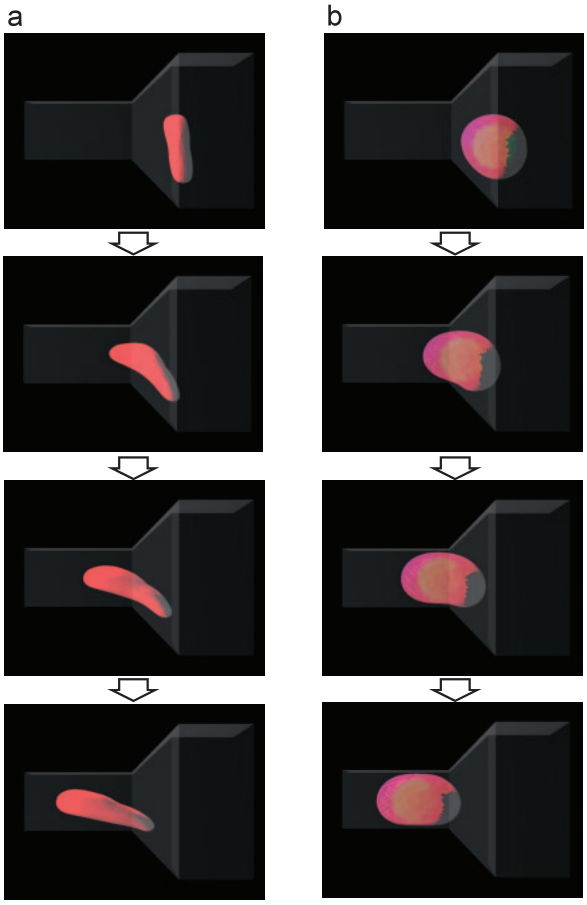


Fig. 16. Snapshots of flow into a 6-μm-square channel. (A) HRBC flows into narrow channel with large deformation. (B) IRBC in the schizont stage also passes through the 6-μm-square channel.

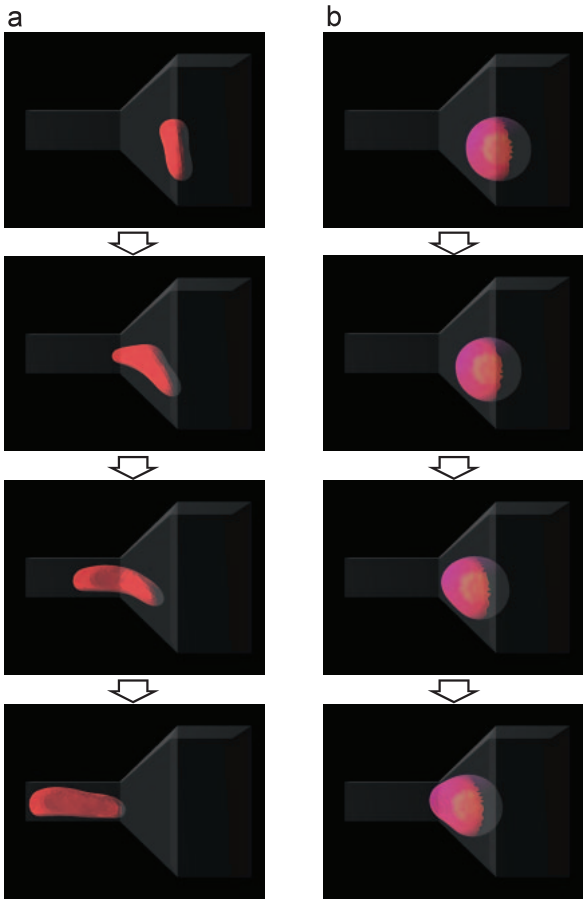


Fig. 17. Snapshots of flow into a 4-μm-square channel. (A) HRBC passes through the narrow channel. (B) IRBC in the schizont stage occludes blood flow.

## 5. Conclusion

In this article, I introduce our recent researches on a novel hemodynamic index for the initiation of cerebral aneurysms focusing on temporal variation of spatial wall shear stress gradient, confocal micro-PTV measurement of blood flow through a stenosed microchannel, and malaria-infected red blood cell mechanics using a particle method.

In section 2, we have proposed a novel hemodynamic index for the initiation of cerebral aneurysms. The result showed that the proposed index had a strong correlation with the location of aneurysm formation. This suggests that the proposed index, GON, may be useful as a hemodynamic index for the initiation of cerebral aneurysms. The reliability of the GON requires examination in other clinical cases as well. This is now under investigation and will be reported elsewhere.

In section 3, individual trajectories of RBCs around the stenosis up to 20% Hct were measured successully. The results revealed that the trajectories of healthy RBCs became asymmetric before and after the stenosis, although the trajectories of tracer particles in pure water were almost symmetric. The asymmetry was

greater in the case of 10% Hct than in 20% Hct. We also investigated the effect of the deformability of RBCs on the cell-free layer by hardening RBCs using a glutaraldehyde treatment. These results indicated that deformability has a considerable effect on the asymmetry of the cell-free layer thickness. Therefore, the motions of RBCs are influenced strongly by the Hct, the deformability, and the channel geometry.

In section 4, we have proposed a numerical model of three-dimensional hemodynamics arising from malaria infection. Particle based spatial discretization and the sub time step time integration can provide us stable computations for the micro scale blood flow involving the interaction with many cells. We performed the stretching of IRBCs and the numerical results agreed well with experimental results. Our model successfully simulated flow of IRBCs into narrow channels. Here, we have not considered the adhesion property of IRBCs. We have already developed an adhesion model [17] and this adhesion model can be applied easily to the current hemodynamic model.

## Acknowledgements

I thank my lab. members: Mr. Kondo, Mr. Fujiwara, Mr. Shimogonya and Dr. Matsuki for conducting researches presented in this paper.

This study was supported by Grant-in-Aid for Scientific Research (S) from the Japan Society for the Promotion of Science (JSPS; No. 19100008) and by a Grant-in-Aid for Young Scientists (A) from the JSPS (No. 19686016). We also acknowledge the support from the 2007 Global COE Program "Global Nano-Biomedical Engineering Education and Research Network Centre" and the "Development and Use of the Next-Generation Supercomputer Project" from the Ministry of Education, Culture, Sports, Science and Technology (MEXT), Japan.

## References

[1] Wang JH, Goldschmidt-Clermont P, Moldovan N, and Yin FC. Leukotrienes and tyrosine phosphorylation mediate stretching-induced actin cytoskeletal remodeling in endothelial cells. *Cell Motil Cytoskeleton* **46**, 137-145, 2000.

[2] Jamous MA, Nagahiro S, Kitazato KT, Satoh K, and Satomi J. Vascular corrosion casts mirroring early morphological changes that lead to the formation of saccular cerebral aneurysm: an experimental study. *J Neurosurg* **102**, 532-535, 2005.

[3] Radaelli AG, Augsburger L, Cebral JR, Ohta M, Rüfenacht DA, Balossino R, Benndorf G, Hose DR, Marzo A, Metcalfe R, Mortier P, Mut F, Reymond P, Socci L, Verhegghe B, and Frangi AF. Reproducibility of haemodynamical simulations in a subject-specific stented aneurysm model—a report on the Virtual Intracranial Stenting Challenge 2007. *J Biomech* **41**, 2069-2081, 2008.

[4] Lima R, Ishikawa T, Imai Y, Takeda M, Wada S, and Yamaguchi T. Radial dispersion of red blood cells in blood flowing through glass capillaries: Role of heamatocrit and geometry. *J Biomech* **41**, 2188-2196, 2008.

[5] Drochona A. Rheology of dilute suspensions of red blood cells: experimental and theoretical approaches. *Eur Phys J AP* **22**, 155-162, 2003.

[6] Faivre M, Abkarian M, Bickraj K, and Stone HA. Geometrical focusing of cells in a microfluidic device: An approach to separate blood plasma. *Biorheology* **43**, 147-159, 2006.

[7] Cooke BM, Mohandas N, and Coppell RL. The malaria-infected red blood cell: structural and functional changes. *Advances in Parasitology* **26**, 1-86, 2001.

[8] Nash GB, O'Brien E, Goldon-Smith EC, and Dormandy JA. Abnormalities in the mechanical properties of red blood cells caused by plasmodium falciparum. *Blood* **74**, 855-861, 1989.

[9] Paulitschke M and Nash GB. Membrane rigidity of red blood cells parasitized by different strains of Plasmodium falciparum. *J Lab Clin Med* **122**, 581-589, 1993.

[10] Lim CT, Zhou EH, and Quek ST. Mechanical models for living cells--a review. *J Biomech* **39**, 195-216, 2006.

[11] Suresh S, Spatz J, Mills JP, Micoulet A, Dao M, Lim CT, Beil M, and Seufferlein T. Connection between single-cell biomechanics and human disease states: gastrointestinal cancer and malaria. *Acta Biomater* **1**, 15–30, 2005.

[12] Lim CT, Zhou EH, Li A, Vedula SRK, and Fu HX. Experimental techniques for single cell and single molecule biomechanics. *Mater Sci Eng C* **26**, 1278-1288, 2006.

[13] Lim CT. Single cell mechanics study of the human disease malaria. *J Biomech Sci Eng* **1**, 82-92, 2006.

[14] Lee GYH and Lim CT. Biomechanics approaches to studying human diseases. *Trends Biotech* **25**, 112-118, 2007.

[15] Shelby JP, White J, Ganesan K, Rathod PK, and Chiu DT. A microfluidic model for single-cell capillary obstruction by Plasmodium falciparum-infected erythrocytes. *PNAS* **100**, 14618-14622, 2003.

[16] Dupin MM, Halliday I, Care CM, and Munn LL. Lattice Boltzmann modelling of blood cell dynamics. *Int J CFD* **22**, 481-492, 2008.

[17] Kondo H, Imai Y, Ishikawa T, Tsubota K, and Yamaguchi T. Hemodynamic analysis of microcirculation in malaria infection. *Ann Biomed Eng*, accepted.

[18] Koshizuka S and Oka Y. Moving-particle semi-implicit method for fragmentation of incompressible fluid. *Nucl Sci Eng* **123**, 421-434, 1996.

[19] Koshizuka S, Nobe A, and Oka Y. Numerical analysis of breaking waves using the moving particle semi-implicit method. *Int J numer meth Fluids* **26**, 751-769, 1998.